Welding in the World
https://doi.org/10.1007/s40194-023-01616-1

RESEARCH PAPER

In situ X-ray phase contrast imaging of the melt and vapor capillary behavior during the welding regime transition on aluminum with limited material thickness

W.-S. Chung[1] · M. Hummel[1] · C. Spurk[2] · A. Häusler[1] · A. Olowinsky[1] · C. Häfner[1,2] · F. Beckmann[3] · J. Moosmann[3]

Received: 10 August 2023 / Accepted: 20 October 2023
© The Author(s) 2023

Abstract
The X-ray phase contrast imaging is a powerful method to understand the fundamental behavior of the melt and keyhole during the laser beam welding process. In this paper, the keyhole-induced vapor capillary formation in the melt pool is investigated by using an adjustable laser beam source. For this purpose, the aluminum A1050 specimen with a thickness of 0.5 mm is molten only with the heat conduction welding regime by using the ring-mode laser beam. Once the specimen is molten through, the core multi-mode laser beam is then applied to vaporize the melt and a transition to keyhole welding regime occurs. Therefore, the core multi-mode laser beam with an intensity value of 33.3 MW/cm^2 is investigated. The correlation between the keyhole-induced vapor capillary and the melt behavior is further investigated in this paper which was recorded with a high sampling rate of 19 kHz. In addition, a theoretical calculation about the keyhole depth is discussed in this paper.

Keywords X-ray phase contrast observation · Laser-spot welding · Transition of welding regime · Keyhole-induced vapor capillary · Melt dynamic

1 Introduction

The laser beam welding process of a material with limited thickness gains its importance due to the increasing demand on the electrical interconnection. The electrical interconnection is not only required for the power electronics or electrical components but also for the interconnection of battery cells in electromobility [1, 2]. Therefore, the laser beam spot-welding process with limited material thickness is investigated in this paper with the in-situ X-ray phase contrast method.

The in situ X-ray imaging of the laser beam welding process enables further understanding of the correlation between the melt and the keyhole dynamic. The extracted information from the X-ray imaging is highly dependent to its given sampling rate and the related clear differentiation between solid, liquid, and gas states during the laser welding process. The in situ observation of the keyhole during the laser beam welding process is investigated by [3] for copper

Recommended for publication by Commission IV - Power Beam Processes

✉ W.-S. Chung
woo-sik.chung@ilt.fraunhofer.de

M. Hummel
marc.hummel@ilt.fraunhofer.de

C. Spurk
christoph.spurk@llt.rwth-aachen.de

A. Häusler
andre.haeusler@ilt.fraunhofer.de

A. Olowinsky
alexander.olowinsky@ilt.fraunhofer.de

C. Häfner
constantin.haefner@ilt.fraunhofer.de

F. Beckmann
felix.beckmann@hereon.de

J. Moosmann
julian.moosmann@hereon.de

[1] Fraunhofer Institute for Laser Technology ILT, Aachen, Germany

[2] Chair of Laser Technology LLT, Aachen, Germany

[3] Institute of Materials Physics, Helmholtz-Zentrum Hereon, Geesthacht, Germany

Published online: 06 November 2023

at high sampling rate of 20 kHz and [4] reached a sampling rate even up to 100 kHz for high-alloy steel [5] recorded the laser beam spot welding process of aluminum at sapling rate with $f = 28$ kHz where process instabilities are monitored by the supervised deep learning. In this paper, the laser beam spot welding process at a high sampling rate of $f = 19128$ Hz is applied to investigate the melt and vapor capillary dynamic for aluminum 1050 A.

A clear transition from the heat conduction welding to keyhole welding regime is investigated. For this purpose, an adjustable laser beam source is used for this experiment to divide the melting and evaporating process. To solely investigate the melt dynamic caused by a keyhole presence, the ring-mode laser beam melts the material with heat conduction, and the core multi-mode laser beam initiates the keyhole welding process. On the basis of the experimental investigation, an equation is proposed to estimate the keyhole depth.

2 Experimental setup

The in situ X-ray phase contrast method is used to examine the melt and keyhole dynamics. Experiments are conducted at the high energy beamline P07 (EH4) of Petra III at the Deutsches Elektronen-Synchrotron DESY in Hamburg. The laser beam spot welding process is demonstrated with a 0.5 mm thick aluminum 1050 A ribbon, which is attached to a milled plate to demonstrate a gap and consequently the limited material thickness. The experimental setup for this investigation is shown in Fig. 1. This setup is developed at the Chair of Laser Technology at RWTH Aachen University and the Fraunhofer Institute for Laser Technology ILT [6].

HighLight FL-ARM Compact laser beam source with a wavelength $\lambda = 1070$ nm is used for this investigation. This adjustable laser beam source allows to control two laser beam sources simultaneously: a ring-mode and multi-mode fiber laser beam. To focus the laser beam at the specimen surface, a *f*-theta lens with a focal length of 163 mm is used. The welding process is conducted at the focal point of the laser beam. The ring-mode laser beam has an outer beam diameter of 536 µm. The multi-mode laser beam is positioned at the center of the ring-mode laser beam and has a beam diameter of 47.92 µm.

The X-ray beam irradiates the interacting zone between the laser beam and specimen at a fixed position. On the opposite side, a scintillator is placed coaxially aligned to the X-ray beam irradiation. So, the transmitted X-ray beam is illuminated on the scintillator. The illuminated laser beam process on the scintillator surface is then recorded with a high-speed camera, which is placed behind the scintillator. As a result, the time-dependent geometrical change of the keyhole and melt is recorded. The sampling rate is set to $f = 19182$ Hz. The recorded X-ray images are image-processed to clearly differentiate the solid, liquid, and vapor states. For this purpose, the X-ray image of the specimen is recorded without the laser beam process and subtracted with the X-ray image during the laser beam process. The imaging process technique from [6, 7] is applied for this paper. An image-processed X-ray image is shown in Fig. 2 to distinguish the different items in the captured X-ray image.

While only the ring-mode laser beam is turned on, a melt pool is visible without a presence of a keyhole. When the multi-mode laser beam is turned on, a penetrating keyhole channel is visible at the center of the melt. Different to the conventional welding process in which the material thickness is considered as semi-infinite, melt boundary outside of the specimen is visible at specimen bottom side.

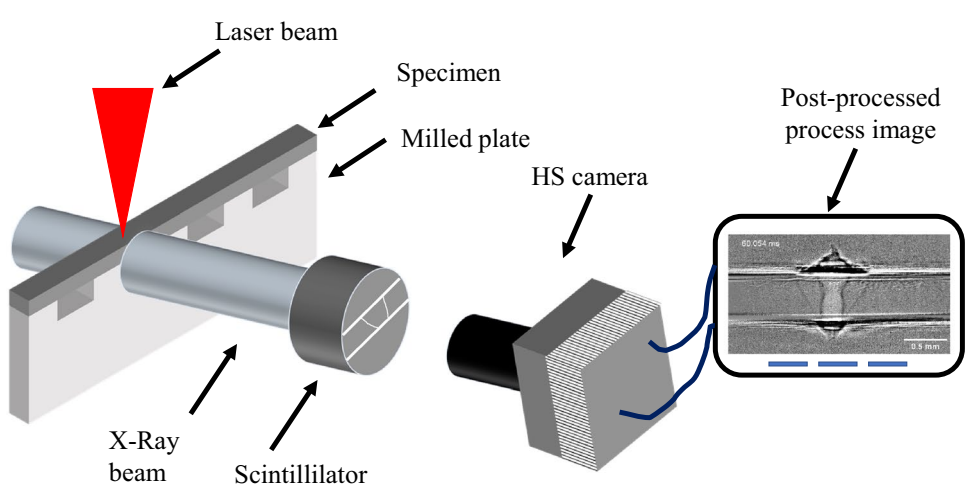

Fig. 1 Experimental setup for the in-situ X-ray phase contrast imaging of laser welding process

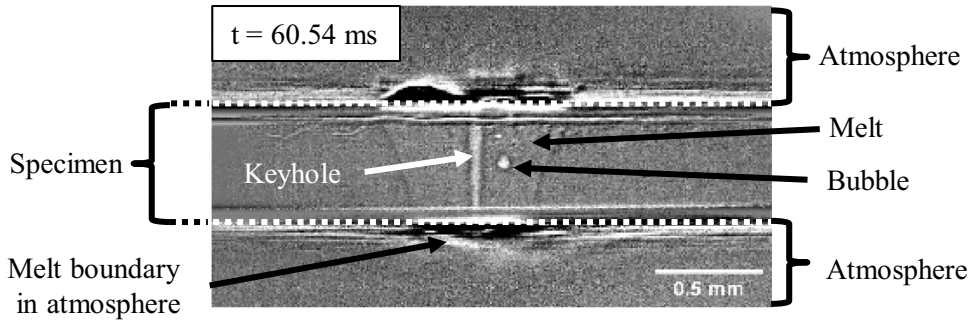

Fig. 2 Exemplary X-ray phase contrast image

3 Results and discussion

3.1 Keyhole-induced vapor capillary development in a melt pool

The ring-mode laser is activated to melt the specimen with a laser beam power of $P_1 = 1000$ W. The irradiation time is set to $t_P = 65$ ms for conducted experiment. This ring-mode laser beam setting leads to a full penetration of the specimen with a heat conduction welding. At $t = 60$ ms, the multi-mode fiber laser beam is turned on with defined laser beam power at the melt center for 5 ms. The investigated laser beam power value for the multi-mode laser beam is $P_2 = 600$ W ($I = 33.3$ MW/cm^2). The image sequence of the X-ray phase contrast imaging is shown in Fig. 3 to visualize the keyhole-induced vapor capillary and melt dynamic.

The melt penetrates towards the specimen bottom solely with heat conduction welding. The melt penetrates into the specimen with a semi-circular melt shape until the lower melt boundary reaches the specimen bottom. As the melt boundary reaches the specimen bottom, the heat accumulation affects the melt shape. Therefore, a semi-circular-shaped melt turns into a truncated cone shape (t = 60 ms). After the melt reaches the specimen bottom, the melt boundary at the specimen bottom widens consequently as the laser beam irradiation continues.

At $t = 60$ ms, the multi-mode fiber laser beam irradiation is initiated at the melt center. A keyhole channel is generated inside of the melt as soon as the multi-mode laser beam is initiated and shows a keyhole-induced vapor capillary expansion until it stabilizes at t = 60.54 ms. During the vapor capillary expansion, the melt is pushed outside the specimen boundary in both directions. At t = 60.05 ms, there is an indication that the keyhole has penetrated through the vapor capillary, which is however clearly observed at t = 60.11 ms. The keyhole penetration reaches the end of the lower melt boundary in the atmosphere. However, as the expanded vapor capillary reaches its maximum and contracts, the pushed melt volume draws back accordingly. Also, the keyhole penetration depth reduces correlated to the position of the melt. As equal laser beam energy and intensity are applied for the multi-mode fiber laser beam irradiation without any further spatial or temporal laser beam modulation, the keyhole penetration depth reduction should be related to the presence of the vapor capillary.

As the expanded vapor capillary draws back, a narrow keyhole channel with a diameter of 60 µm penetrates the melt (t > 60.27 ms). In spite of continuous laser beam irradiation at constant laser beam intensity value, no further keyhole-induced vapor capillary expansion and therefore a melt is pushed outside the specimen boundary.

The volume of pushed-out melt increases, as the vapor capillary area in the specimen increases. However, as the expanded vapor capillary reaches its maximum value and contracts, the melt in the atmosphere draws back accordingly.

The balanced pressure equilibrium during the heat conduction welding process is interrupted by the sudden presence of the multi-mode laser beam. As a consequence, the melt rapidly vaporizes along the penetrating laser beam, which leads to a keyhole channel inside the melt. The keyhole channel however does not fully penetrate the melt. The inertia of the vapor pressure caused by evaporation at the keyhole wall leads to a vapor capillary expansion [8]. As the vapor pressure p_v exceeds the melt surface tension pressure p_γ, the melt is pushed outside the specimen boundary and results into an up as well as down melt streaming. The melt surface tension pressure is dependent to its surface tension and radius (Eq. 1).

$$p_{\gamma,i} = \frac{F_{\gamma,i}}{A} = \frac{2 \bullet \pi \bullet r_i \bullet \gamma_i \bullet \cos\theta}{\pi \bullet r_i^2} \tag{1}$$

$p_{\gamma,i}$ is the surface tension pressure of the melt [kPa]; $F_{\gamma,i}$ is the surface tension force [N]; r_i is the melt radius [mm]; γ_i is the surface tension of melt [N/mm]; θ is the fluid melt angle [°]; A is the pressure acting melt area [mm^2].

At the pressure equilibrium state (t = 60 ms), the melt radius is measured by examining the X-ray image and the fluid melt angle is considered as 0° for maximum surface tension force [9]. The surface tension is temperature dependent. Assuming a homogenous melting temperature

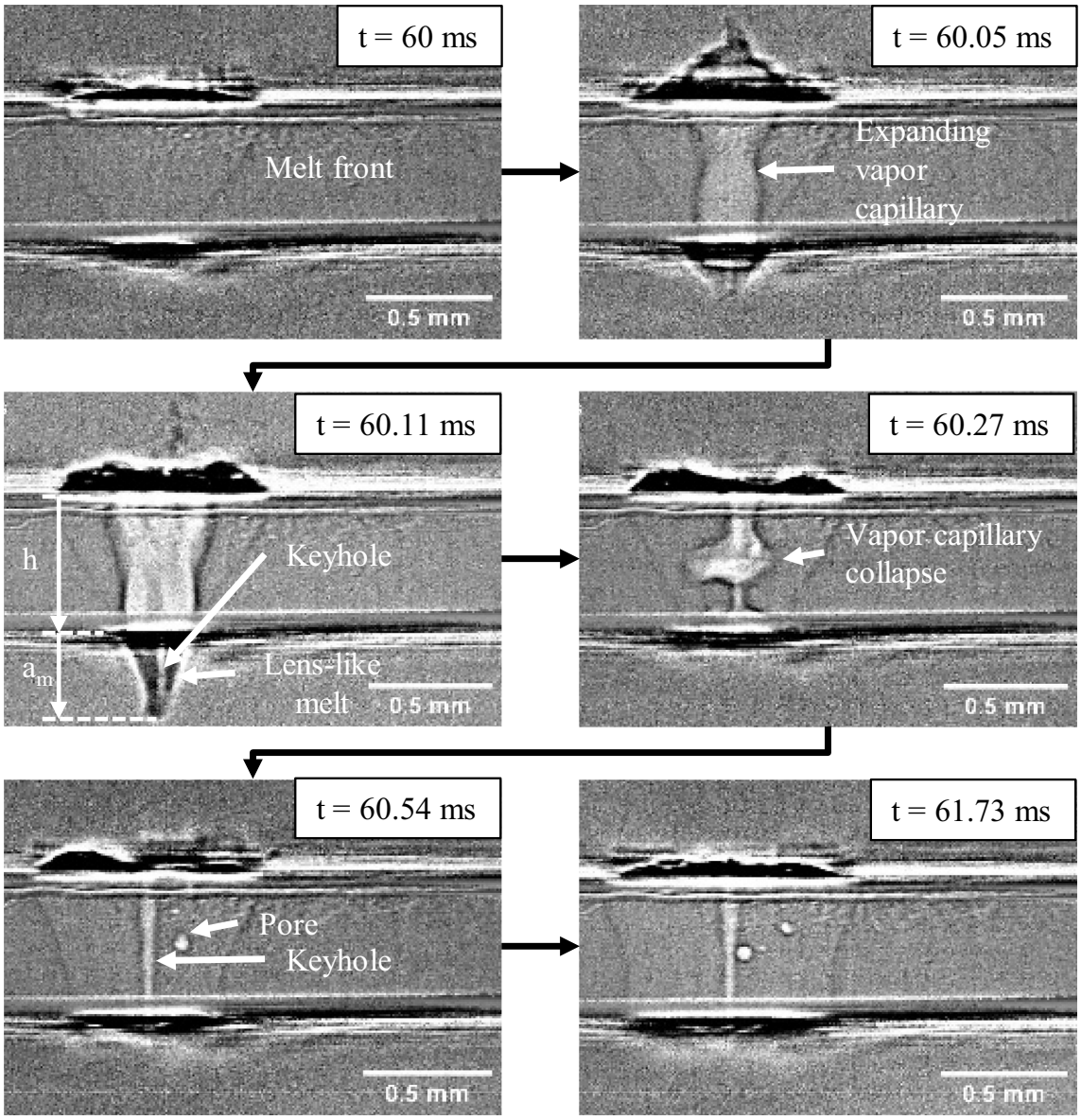

Fig. 3 Image sequence of the x-ray phase contrast observation of the laser spot welding process for the following parameter: P_P = 1000 W; t_P = 65 ms; P_D = 600 W; t_P = 5 ms (starting from t = 60 ms); f = 19128 fps. h, material thickness [mm]; a_m, melt amplitude [mm]

at the melt boundary, the surface tension of aluminum melt boundary is 875 mN/m according to [10]. The calculated surface tension pressure for the upper melt boundary is 3.5 kPa (radius $r_{m,t}$ =0.5 mm) and for the lower melt boundary is 10.29 kPa ($r_{m,b}$ = 0.17 mm). The vapor pressure and the pressure forces p_f acting on the keyhole front producing a melt flow component parallel to the laser beam axis are difficult to distinguish [8]. However, a sum of the mentioned pressure values can be estimated by considering the surface tension pressure of the melt spike at the specimen bottom. In spite of the maximally expanded vapor capillary, the melt spike is only stretched without melt spatter ejection (t = 60.108 ms). Therefore, when the pressure equilibrium at that moment is considered, an estimation of the vapor pressure and the pressure force acting on the keyhole front can be determined (Fig. 4).

The melt radius of the stretched melt spike at the lower melt boundary is measured with r_m = 41.5 µm. Also, as the keyhole front is positioned proximately to the melt–atmosphere boundary, the melt temperature is reasonably higher than the melting temperature. The surface tension value of aluminum liquid temperature at 1550 K is 800 mN/m [10]. The surface tension value at higher temperature is not found in the literature. [11] has reported that the impact of the gravitational force at the melt spike is negligible compared to the vapor pressure due to its

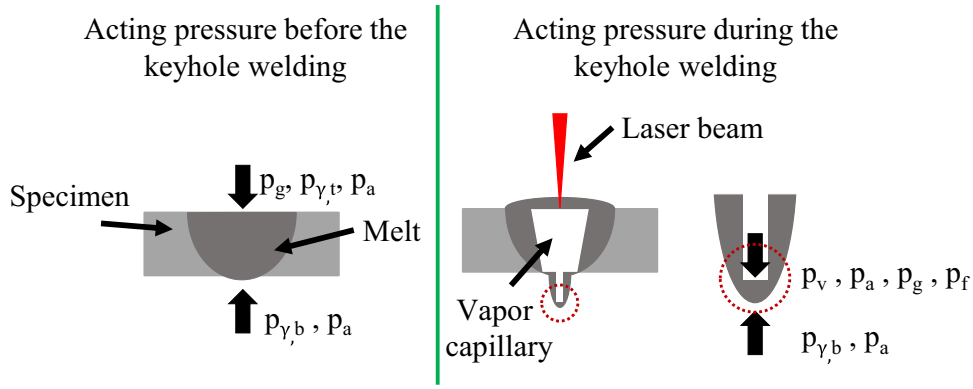

Fig. 4 Schematic representation of the pressure equilibrium at maximally expanded vapor capillary

negligible mass. As a result, a pressure equilibrium at melt spike can be simplified to the following Eq. 2.

$$p_v + p_f = p_{\gamma,b} \tag{2}$$

p_v is the vapor pressure [N/mm^2]; p_f is the keyhole front pressure [N/mm^2]; $p_{\gamma,b}$ is the surface tension pressure [N/mm^2].

The calculation surface tension pressure at the melt spike with given value is 38.5 kPa. In other words, the initiation of a core multi-mode laser beam with a laser beam intensity 33.3 MW/cm^2 induces a vapor- and keyhole front pressure of Δ33.35 kPa at the lower melt boundary. The separated determination between the vapor pressure and the pressure force is not further discussed within this paper.

After the keyhole-induced vapor capillary expands to its maximum volume, the vapor capillary volume decreases and the melt draws back. Once the pressure equilibrium is reached, only a narrow vapor capillary fully penetrates the melt and spatters are ejected occasionally without down-streaming melt. Therefore, the described vapor capillary expansion is only temporally. The remaining dwell time for the expanded vapor capillary is $t_{Dw} = 162$ µs.

3.2 Approximation of the keyhole depth to the applied laser beam intensity

The keyhole channel is observed for the investigated intensity value (33.3 MW/cm^2) in the previous sub-section. For $t = 60.11$ ms, the keyhole has penetrated the specimen thickness ($h = 0.5$ mm). However, the keyhole penetration depth z_k did not exceed the lower end of the pushed out melt amplitude a_m ($z_k \leq h+a_m$). The theoretical relation between the keyhole depth and the applied intensity is discussed in this sub-section (refer to Fig. 3).

The melt pool is generated solely through the heat conduction welding until $t = 60$ ms. The following multi-mode laser beam is therefore theoretically positioned at the melt pool surface ($z = 0$) for the initial phase. The keyhole penetration depth on a described specimen can be estimated with the energy balance equation at the laser spot.

(Leaning on [12])

$$A_L \bullet I_E = \rho \bullet L_v \bullet \frac{\partial z_k}{\partial t} - K \bullet \left(\frac{\partial T}{\partial z}\right)_{z=0} \tag{3}$$

A_L is the absorption degree [-]; I_E is the elevated laser beam intensity [MW/cm^2]; ρ is the density [kg/m³]; L_v is the latent heat of evaporation [J/kg]; $\frac{\partial z_k}{\partial t}$ is the keyhole penetration velocity [m/s]; K is the thermal conductivity [W/mK]; $\frac{\partial T}{\partial z}$ is the temperature gradient at the welding front [K/m].

According to [12], the absorbed elevated laser beam intensity is a subtraction between the heat and vaporize and melt the specimen. When the welding process is proceeded only with a single laser beam source, two laser beam intensity level is required to achieve a heat conduction welding and keyhole welding regime [7]. In this case, the elevated laser beam intensity is defined as a subtracted intensity value of the two intensity values. However, for the adjustable laser beam source, two laser beam sources are used for each purpose: ring-mode laser for melting and multi-mode laser for vaporization. Therefore, the laser beam intensity of the multi-mode fiber laser beam is considered as elevated laser beam intensity for Eq. 3. Knowing the amount of the absorbed laser beam intensity, the temperature gradient at the welding front is to be determined for the keyhole penetration depth estimation. The transient 1-dimensional heat conduction (Eq. 4) is applied to express the temperature distribution inside of the melt over the laser beam irradiation time:

$$\frac{1}{\alpha} \bullet \frac{\partial T}{\partial t} = \frac{\partial^2 T}{\partial z^2} \tag{4}$$

α is the thermal diffusivity [m²/s]; $\frac{\partial T}{\partial t}$ is the temperature distribution [K/s]

The temperature distribution in the melt can be further expressed with the keyhole penetration depth over the time which is influenced by the temperature change over the

depth of the melt. So, the rewritten Equation is shown in the equation below:

$$-\frac{1}{\alpha} \bullet \frac{\partial z_k}{\partial t} \bullet \frac{dT}{dz} = \frac{d^2 T}{dz^2} \tag{5}$$

$\frac{dT}{dz}$ is the temperature distribution over the melt [K/s].

The boundary conditions for the temperature distribution are considered as an ideal case after the heat conduction welding at $t = 60$ ms: The melt surface starts to vaporize at $z = 0$ with $T = T_v$, and the melt lower side ($z = h$) has just reached its melting temperature with $T = T_m$. Considering the boundary conditions, the solution for Eq. 5 of the temperature distribution over the melt is calculated. As a result, the temperature gradient at the keyhole front in penetration direction can be substituted into the energy balance to Eq. 6.

$$A_L \bullet I_E = \rho \bullet L_v \bullet \frac{dz_k}{dt} + \rho \bullet c_p \bullet \frac{dz_k}{dt} \bullet \left(T_v - T_m\right) \tag{6}$$

c_p is the specific heat capacity [J/gK]; T_v is the evaporization temperature [K]; T_m is the melting temperature [K].

The equation above is sorted out to the expression of the vapor penetration velocity and the integration of the sorted equation leads to an equation of the keyhole penetration length z_k as shown below.

$$z_k = \frac{\mathrm{A_L} \bullet \mathrm{P} \bullet \mathrm{t}}{\pi \bullet \mathrm{r_s^2} \bullet \rho \bullet \left[\mathrm{L_v} + \mathrm{c_p} \bullet \left(\mathrm{T_v} - \mathrm{T_m}\right)\right]} \tag{7}$$

r_s is the laser beam radius [mm²]; P is the laser beam power [W]; t is the irradiation time [s].

Based on the equation above, the keyhole penetration depth can be estimated by the absorbed elevated laser beam intensity and irradiation time of the multi-mode laser beam. The required elevated intensity value and the duration until the keyhole penetrates given melt thickness can be estimated in Fig. 5. The calculation is conducted with thermophysical material properties of aluminum listed in Table 1.

The keyhole penetration depth increases rapidly with increasing irradiation duration and absorption degree. On the basis of this calculation, the keyhole development within the material can be estimated dependent to the absorbed laser beam intensity. Considering the difference between two calculated absorption degree, keyhole penetration depth is highly influenced by the absorption degree of the laser beam at the melt.

Table 1 Thermophysical material properties of aluminum [10]

Density ρ [g/cm²]	Latent heat of vaporization L_V [J/K]	Specific heat capacity c_p [J/gK]	Evaporization temperature T_V [K]	Melting temperature T_m [K]
2.357 (@T = 973 K)	10500	1.18	2743	930.15

3.3 Validation

The validation of Eq. 7 is conducted by comparing the measured keyhole depth from Fig. 3 at the irradiation time for t_D = 108 µs to the calculated keyhole depth value. For the calculation of the keyhole depth, an accurate estimation of the absorption degree during the keyhole welding is required. Therefore, the incoupling degree is considered for the validation which is suggested by Beck.

Within the keyhole, the laser beam is reflected multiple times, and for each encountering on the keyhole wall, a partial laser beam energy is absorbed at the wall. The total amount of absorbed laser beam energy through the Fresnel absorption is not only dependent to the absorption degree of the material but strongly dependent to the shape of the keyhole [13]. The total amount of absorbed laser beam energy within the keyhole is also called as an incoupling degree η_A and can be estimated with an equation for a cone-shaped vapor capillary [13]:

$$\eta_A = A_L \bullet \frac{1 + (1 - A) \bullet \frac{1}{2 \bullet S_v} \bullet \left(1 - \frac{1}{2 \bullet S_v}\right)}{A_L \bullet \left(1 - \frac{1}{2 \bullet S_v}\right) + \frac{1}{2 \bullet S_v}} \tag{8}$$

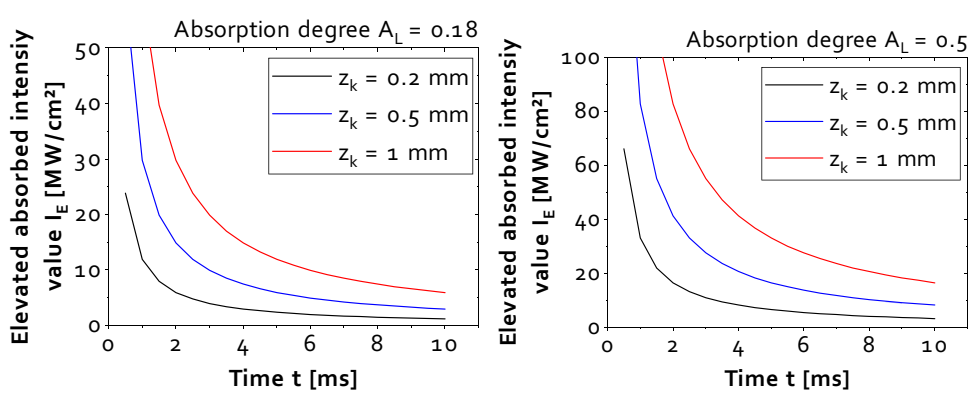

Fig. 5 Calculated keyhole penetration depth dependent on the laser beam intensity and absorption degree

η_A is the incoupling degree [-]; A_L is the absorption degree [-]; S_v is the aspect ratio of capillary [-].

This estimation assumes that the keyhole diameter d_{cap} is equally large as the laser spot diameter d_s, and the aspect ratio of keyhole is defined as $S_v = z_{cap}/d_{cap}$ where z_{cap} is the keyhole depth, respectively [13]. The keyhole geometry can be measured from the X-ray image, and the aspect ratio of keyhole is S_v calculated as 16.6. The determined aspect ratio of keyhole leads to an incoupling degree of 90.38%. At given laser beam intensity value ($I = 33.3$ MW/cm²), the solution of Eq. 7 with the material properties from Table 1 leads to a keyhole depth of $z_k = 1.08$ mm. Considering the measured keyhole depth with $z_k = 827$ µm, the calculated value differs by 23%.

4 Conclusion and outlook

In this paper, a laser beam spot welding process is investigated on an aluminum with a thickness of 0.5 mm. A clear differentiation of the melting and vaporizing process is conducted by using an adjustable laser beam source. On the basis of the X-ray imaging with high sampling rate $f = 19182$ Hz, the melt dynamic caused by the keyhole-induced vapor capillary expansion is observed. The pressure equilibrium of the melt is interrupted by a sudden presence of the keyhole. Along the penetrating keyhole, the melt vaporizes at keyhole wall and induces a vapor pressure. The inertia of the vapor pressure expands its volume and overcomes the surface tension pressure of the melt boundary resulting a melt spike. The vapor and keyhole front pressure induces a pressure difference of Δ33.35 kPa which leads to the lower melt spike at $t = 60.108$ ms. After the expanded vapor capillary reaches its maximum value, the melt draws back and a narrow keyhole fully penetrates the melt. The keyhole diameter is measured to 60 µm which is comparable to the core multi-mode laser beam diameter of 49 µm. On the basis of the one-dimensional energy balance equation, the keyhole depth is approximated with $z_k = 1.08$ mm. The validation of the theoretical calculation divers 23% compared to the measured keyhole depth, which is $z_k = 0.827$ mm.

As for the outlook, the correlation between melt dynamic and keyhole-induced vapor capillary expansion should be further understood. For this purpose, an even higher sampling rate is still required. By increasing the sampling rate up to 75000 Hz, a detailed development of the vapor capillary is expected to be recorded. Hence, the differentiation between the vapor pressure and the keyhole front pressure parallel to the laser beam could be determined. Furthermore, the temperature at the melt spike edge could be more precisely determined by placing different metals below the aluminum specimen with a defined gap. As the dwell time for the melt spike is limited, the heat transfer to the underlying metal can be estimated. If the melt spike contacts the metal surface and forms a weld joint within estimated dwell time, the temperature at the melt spike can be determined [14]. Also, a simulation-assisted investigation can be performed to understand the vapor capillary shape during the expansion.

Acknowledgements The presented investigations were carried out at RWTH Aachen University within the framework of the Collaborative Research Center (No. SFB1120-236616214) "Bauteilpräzision durch Beherrschung von Schmelze und Erstarrung in Produktionsprozessen" and funded by the Deutsche Forschungsgemeinschaft e.V. (DFG, German Research Foundation). The sponsorship and support are gratefully acknowledged.

Funding Open Access funding enabled and organized by Projekt DEAL.

Declarations

Competing interests The authors declare no competing interests.

Open Access This article is licensed under a Creative Commons Attribution 4.0 International License, which permits use, sharing, adaptation, distribution and reproduction in any medium or format, as long as you give appropriate credit to the original author(s) and the source, provide a link to the Creative Commons licence, and indicate if changes were made. The images or other third party material in this article are included in the article's Creative Commons licence, unless indicated otherwise in a credit line to the material. If material is not included in the article's Creative Commons licence and your intended use is not permitted by statutory regulation or exceeds the permitted use, you will need to obtain permission directly from the copyright holder. To view a copy of this licence, visit http://creativecommons.org/licenses/by/4.0/.

References

1. Haddad E, Chung WS, Katz O, Helm J, Olowinsky A, Gillner A (2022) Laser micro welding with fiber lasers for battery and fuel cell based electromobility. J Adv Joining Processes 5:100085. https://doi.org/10.1016/j.jajp.2021
2. Dimatteo V, Ascari A, Liverani E, Fortunato A (2022) Experimental investigation on the effect of spot diameter on continuous-wave laser welding of copper and aluminum thin sheets for battery manufacturing. Opt Laser Technol 145:107495
3. Schricker K, Schmidt L, Friedmann H, Diegel C, Seibold M, Hellwig P, Chen Y (2022) Characterization of keyhole dynamics in laser welding of copper by means of high-speed synchrotron X-ray imaging. Procedia CIRP 111:501–506
4. Chen Y, Clark S, Leung C, Sinclair L, Marussi S, Olbinado M, Lee P (2020) In-situ Synchrotron imaging of keyhole mode multi-layer laser powder bed fusion additive manufacturing. Appl Mater Today 20:100650
5. Shevchik S, Le-Quang T, Meylan B, Farahani F, Olbinado M, Rack A, Wasmer K (2020) Supervised deep learning for real-time quality monitoring of laser welding with X-ray radiographic guidance. Sci Rep 10(1):3389
6. Hummel M, Külkens M, Schöler C, Schulz W, Gillner A (2021) In situ X-ray tomography investigations on laser welding of copper with 515 and 1030 nm laser beam sources". J Manuf Processes 67:170–176

7. Chung W, Häusler A, Hummel M, Olowinsky A, Gillner A, Beckmann F, Moosmann J (2021) In-situ x-ray phase contrast observation of the full penetration spot welding on limited aluminum material thickness. J Laser Appl 34(4):42019
8. Berger P, Hügel H (2013) Fluid dynamic effects in keyhole welding – an attempt to characterize different regimes. Phys Procedia 41:216–224
9. Dijken D, Hoving W, De Hosson J (2003) Laser penetration spike welding: a microlaser welding technique enabling novel product designs and constructions. J Laser Appl 15(1):11–18
10. Leitner M, Leitner T, Schmon A, Aziz K, Pottlacher G (2017) Thermophysical properties of liquid aluminum. Metallurgical and Materials Transactions. A, Physical Metallurgy and Materials. Science 48(6):3036–3045
11. Britten S (2017) Bauteilschonende Verbindungstechnik Auf Metallisierungen Durch Moduliertes Laserstrahlschweißen. Apprimus Verlag, Dissertation
12. Naim Md I (2012) Nd : YAG laser welding for photonics devices packaging. IntechOpen 2012:77
13. Beck M (1996) Modellierung des Lasertiefschweißens. In: Hügel H (ed) Laser in der Materialbearbeitung - Forschungsberichte des IFSW. Teubner Verlag, Dissertation
14. Chung W, Haeusler A, Olowinsky A, Gillner A, Poprawe R (2018) Investigation to increase the welding joint area with modulated laser beam welding over gap. J Laser Micro Nanoeng 13(2):117–125

Publisher's note Springer Nature remains neutral with regard to jurisdictional claims in published maps and institutional affiliations.